

This is the accepted manuscript made available via CHORUS. The article has been published as:

Controlling phase separation in vanadium dioxide thin films via substrate engineering

Stephanie N. Gilbert Corder, Jianjuan Jiang, Xinzhong Chen, Salinporn Kittiwatanakul, I-Cheng Tung, Yi Zhu, Jiawei Zhang, Hans A. Bechtel, Michael C. Martin, G. Lawrence Carr, Jiwei Lu, Stuart A. Wolf, Haidan Wen, Tiger H. Tao, and Mengkun Liu

Phys. Rev. B **96**, 161110 — Published 23 October 2017

DOI: [10.1103/PhysRevB.96.161110](https://doi.org/10.1103/PhysRevB.96.161110)

Controlling phase separation in vanadium dioxide thin films via substrate engineering

Stephanie N. Gilbert Corder¹, Jianjuan Jiang², Xinzhong Chen¹, Salinporn Kittiwatanakul³, I-Cheng Tung⁴, Yi Zhu⁴, Jiawei Zhang¹, Hans A. Bechtel⁵, Michael C. Martin⁵, G. Lawrence Carr⁶, Jiwei Lu³, Stuart A. Wolf^{3,7}, Haidan Wen^{4,†}, Tiger Hu Tao^{2,8,†}, Mengkun Liu^{1,†}

1. Department of Physics, Stony Brook University, Stony Brook, New York 11794, USA
2. State Key Laboratory of Transducer Technology, Shanghai Institute of Microsystem and Information Technology, Chinese Academy of Sciences, Shanghai 200050, China
3. Department of Materials Science and Engineering, University of Virginia, Charlottesville, Virginia 22904, USA
4. Advanced Photon Source, Argonne National Laboratory, Argonne, Illinois 60439, USA
5. Advanced Light Source, Lawrence Berkeley National Laboratory, Berkeley, California 94720, USA
6. NSLS-II Photon Sciences, Brookhaven National Laboratory, Upton, NY 11973, USA
7. Department of Physics, University of Virginia, Charlottesville, Virginia 22904, USA
8. Department of Mechanical Engineering the University of Texas at Austin, Austin, TX 78712, USA

[†] E-mail: mengkun.liu@stonybrook.edu; tiger.tao@austin.utexas.edu; wen@aps.anl.gov

The strong electron-lattice interactions in correlated electron systems provide unique opportunities for altering the material properties with relative ease and flexibility. In this work, we use localized strain control via a focused-ion-beam-patterning of TiO₂ substrates to demonstrate that one can selectively engineer the insulator-to-metal transition temperature, the fractional component of the insulating and metallic phases, and the degree of optical anisotropy down to the length scales of the intrinsic phase separation in VO₂ thin films without altering the quality of the films. The effects of localized strain control on the strongly correlated electron system are directly visualized by state-of-the-art IR near-field imaging and spectroscopy techniques and X-ray micro-diffraction measurements.

Understanding, designing, and manipulating phase transitions at microscopic length scales in a chemically homogeneous system is a central goal of strongly correlated electron material (SCEM) research. Several pathways exist for modifying the properties of SCEM and controlling their phase separation at relevant length scales. Such paths include local electric-field gating [1–5], ion beam implantation [6], and light-induced phase transitions [7–9]. The electric-field and light induced effects alter the local phases with inhomogeneous carrier doping or localized heating while ion implantation allows for spatially-selective phase engineering by introducing local defects and substitutions of atoms. While these methods have generated considerable interest for controlling SCEM, they have their own limitations: the high gate voltages often require the fabrication of nano-electrodes, making control of local fields across macroscopic length scales difficult. Ion implantation can induce local structural defects, which may add extrinsic factors to the phase transitions. Light-induced inhomogeneities are restricted to the diffraction-limited spot size and are often transient effects – the inhomogeneities disappear when the light is switched off. In contrast to previous methods which rely on directly altering the SCEM films, we demonstrate a different route for controlling phase inhomogeneities down to the nano-scale: interface facet engineering. As will be shown below, this new method possesses **several unique advantages for modifying the local properties in SCEM including reduced chemical defects, no post-fabrication processing, and direct control of the extent of the anisotropy and inhomogeneity.**

This research is motivated by previous investigations of the nanoscale phase separation of vanadium dioxide (VO_2) thin films at elevated temperatures [5,10–12]. IR near-field imaging studies revealed that the phase transition temperature and the microscopic phase separation patterns of VO_2 films vary considerably when grown on different substrates [10,13]. **These distinct substrate orientation- and film thickness-dependent mesoscopic patterns in highly oriented transition metal oxide thin films originate from the epitaxial strain due to lattice mismatch between the film and substrate [10,14–16].** For

example, in VO₂ films on a (110)_R TiO₂ substrate with an in-plane rutile c_R axis, stripe-like unidirectional phase separations are evident [11]. These metallic stripes can extend throughout the entire sample for a typical sample size of around 10 mm × 10 mm. The width and periodicity of the stripes are typically sub-μm, depending on the sample thickness [11]. In VO₂ films on sapphire substrates (e.g. c-Al₂O₃), however, a randomized metallic nucleation takes place rather than pattern formation [17,18]. While in VO₂ films on (001)_R TiO₂ substrates, the mesoscopic self-organized phase inhomogeneities are totally absent [10]. The substrate-dependent phase inhomogeneities for the different films are mainly the result of distinct elastic coupling and epitaxial strain between the VO₂ and the substrate lattice. The complex, self-organized elastic interactions at the interface lead to variations in transition temperature and electronic phase separation in the VO₂ films.

The epitaxial strain initiated local texture formation provides an opportunity for nano-engineering of functional SCEM materials. By introducing nanoscale roughness and exposing different facets of the substrates before depositing the films, one can effectively control the interfacial strain and thus the phase transition properties of the subsequent SCEM films. We demonstrate that the strain-induced electronic anisotropy in VO₂ can be locally transformed into isotropic conducting regions in a controlled manner. The engineered mixed electronic phases are studied with nano-scale resolution using near-field imaging and spectroscopy. **The crystal structure of the VO₂ film is further characterized with micro-x-ray diffraction (μ-XRD) and reciprocal space mapping to provide a direct characterization of the local lattice parameters and structural phase composition.**

We use a focused ion beam (FIB) to create checkerboard patterns on (110)_R TiO₂ substrates before VO₂ film deposition. Within the patterned region, 50% of the surface is masked, and the remaining 50% is exposed to the beam as squares. The typical applied voltage for the ion beam lithography is ~30 keV, with the beam current ~24 pA (strata FIB 201, FEI Co., Ga ions). Patterns of different sizes (e.g., 200 nm, 500 nm, 1 μm, 5 μm) and

different alignment angles (e.g., 0° , 30° , 45° with respect to the $(001)_R$ axis) are created on the same substrate. The entire fabrication procedure is schematically shown in Figure 1 (a) and the actual patterns can be seen in the [Supplemental Materials Figure S1 and S2 \[19\]](#). The FIB etches the substrate surface to a depth of a few nm to a hundred nm. The high energy ions roughen the surface of the TiO_2 and modify the structure by exposing different crystal facets in the TiO_2 along their collision path. The size of the structurally modified region depends on the dosage of the incident ion beam and the degree of beam spot dispersion [20]. [At high doses, ion the bombardment from FIB milling can relieve the implantation-induced substrate strain through localized lattice distortion \[21\].](#)

A VO_2 thin film is then grown on the patterned substrate using reactive bias target ion beam deposition at a substrate temperature of 400°C under 5.5 sccm Ar/O_2 80/20 mixture flow. [The details on the sample growth and characterization can be found in the Supplemental Materials Figure S3 \[19\] and references \[22,23\].](#) The VO_2 film thickness is estimated to be 71 nm with <5 nm variation across the entire pattern. As a result of the FIB patterning, the VO_2 displays increased roughness in the checkerboard regions as compared to the single crystal thin film in the unpatterned areas (see the Supplemental Materials [Figure S4 \[19\]](#)). The disruption of the $(110)_R$ TiO_2 surface alters the orientation of the VO_2 in the patterned regions and is shown schematically as an interface cross section in Figure 1 (b).

In order to probe the electronic properties at the nano-scale, scattering scanning near-field optical microscopy ([s-SNOM; NT-MDT NTEGRA-IR](#)) is used to [image the IR properties of the samples at single frequencies \(10-11 \$\mu\text{m}\$ \) or collect spectra at specific locations with a broadband light source \(ALS SINS beamline\).](#) The infrared near-field apparatus has ~ 10 nm spatial resolution ($\sim \lambda/1000$) - far beyond the light diffraction limit ($\sim \lambda/2$) - ensuring optical imaging and spectroscopic identification without integrating the information from mixed phases [\[24–32,17,33–36\]](#). This fine resolution is especially helpful in studying phase

transitions close to the critical temperature since the areal averaging in traditional far-field measurement techniques can hinder the data interpretation in systems with complex phases. s-SNOM is able to distinguish different phases in the coexistence region and directly accesses fundamental properties of the materials, enabling direct mapping of the IR electronic structure at extreme subwavelength scales [34–36]. The unique sensitivity of s-SNOM facilitates the strain nano-engineering presented in this study.

In order to probe the local crystallographic structure variations in the VO₂ film, μ -XRD is performed using a monochromatic 11 keV x-ray beam with sub-micron resolution at the 7-ID-C beamline of the Advanced Photon Source [37]. The x-ray beam is focused down to a spot size of 1 μ m (FWHM) by a Fresnel zone plate in our experiments, which has sufficient spatial resolution to characterize the 5 μ m \times 5 μ m checkerboard patterns. Scanning x-ray imaging by diffraction intensity at the film peak position and local x-ray scattering specular scans are acquired at different temperatures from 295 K to 350 K. The variation with strain of the spatial lattice constants for different phases are obtained by analyzing the XRD specular scans.

We first studied the VO₂ films on patterned (110)_R TiO₂ substrates at room temperature. Three regions on the sample can be identified: the unpatterned single crystal VO₂ (UP), the substrate-unetched region of the pattern (UE), and the substrate-etched region of the pattern (EP). These three regions are clear in AFM topography, which is shown in Figure 2 (a). The line profile in Figure 2 (b) shows the height variation is within several nm, as the result of the substrate etching. Near-field microscopy is performed on the same area simultaneously with the AFM measurements. At room temperature, very little contrast is evident in the third harmonic near-field signal (Figure 2 (c), S₃ measured at 10 μ m), indicating the entire sample is insulating. The exposed crystal facets in the substrate-etched patterned region (EP) lower the local transition temperature, resulting in a slightly higher optical conductivity compared to the unpatterned region (UP). The three regions identified in the topography are examined with

broadband near-field FTIR in Figure 2 (d) using the SINS synchrotron beamline at the ALS, Berkeley [32]. The second harmonic (S_2) of the near-field response of a known phonon mode of VO_2 [38] is shown to decrease by $\sim 15\%$ in the substrate-etched patterned region (EP), indicating a variation in the local crystal orientation due to the strain nano-engineering. To characterize the local crystallinity, a μ -XRD intensity map of the patterned region at $(022)_M$ peak is shown in Figure 2 (e), highlighting the change of the Bragg peak as a result of the substrate patterning. The three representative locations of the pattern are indicated in (e) and the corresponding diffraction peaks are shown in (f). Moving from the unpatterned area (UP) to the substrate-unetched area within the pattern (UE), it is clear the diffraction intensity decreases. Moving into the substrate-etched patterned area (EP), the diffraction intensity is significantly reduced (Figure S5 in the Supplemental Materials [19]). The reduction of diffraction intensity is not attributed to polycrystallization as the VO_2 powder diffraction ring was not observed on the X-ray area detector (PILATUS 100K, see Figure S6 in the Supplemental Materials [19]). Nor can the reduction in diffraction intensity be attributed to amorphization, as indicated by Raman measurements (Supplemental Materials Figure S7 [19]), which show a reduction in signal of well-known modes, consistent with previous reports [39-42]. Instead, the reduced diffraction intensity in area (EP) suggests that the out-of-plane crystal axis of the majority VO_2 film on the etched TiO_2 substrate is not aligned along $(110)_R$. Although these regions of the VO_2 film are not aligned, their orientations are not randomized either, due to the lack of a powder diffraction ring. The results shown in Figure 2 indicate that the modified interface alters the local epitaxy of the VO_2 film, producing regions of single crystal VO_2 (unpatterned (UP)), less-aligned VO_2 (substrate-unetched region within the pattern (UE)), minimally-aligned VO_2 (substrate-etched pattern (EP)), and the intermediate areas at the border between the different regions. In addition, we find two monoclinic $(022)_M$ Bragg peaks, M and M', at room temperature which can be resolved with a double Gaussian fitting (see the Supplemental Materials Figure S8 [19]). The M peak is close

to the bulk value of monoclinic VO_2 (022)_M peak while the M' peak has a smaller out-of-plane lattice constant due to epitaxial strain. The peak width of the M phase gradually increases from region (UP) to (EP), suggesting the coherence length (as measured by the inverse of the Bragg peak width and defined as the length over which crystalline order is maintained) of the M phase along the out-of-plane direction gradually decreases from region (UP) to (EP). This reduction of the coherence length of the M phase with patterning is consistent with a relaxed (unstrained) VO_2 film, while the strained VO_2 film component M' shows no discernable coherence length differences in these three regions (see the Supplemental Materials Figure S8 for details [19]).

The temperature-dependent s-SNOM characterization of the infrared properties of the VO_2/TiO_2 patterns, crucial for future applications of the proposed substrate nano-engineering technique, is presented in Figure 3 where the insulating conductivity is in red and the metallic conductivity is in cyan. Figure 3 (a)-(f) demonstrates the response of a $5\ \mu\text{m} \times 5\ \mu\text{m}$ checkerboard and (g)-(l) shows a $1.5\ \mu\text{m} \times 1.5\ \mu\text{m}$ checkerboard. The near-field images at $11\ \mu\text{m}$ demonstrate that the VO_2 on the etched regions of the TiO_2 substrate (region (EP)) undergo the IMT at lower temperatures than the unpatterned, highly oriented region of the film (region (UP)). Region (EP) also lacks the characteristic anisotropic metallic stripes (cyan color) evident in the region (UP). This is due to the fact that the film on the unetched TiO_2 surface is subject to a highly oriented epitaxial growth, yielding a typical stripe-like insulator to metal phase transition as observed in strained single crystalline thin films [10,11,15], while the region of the film grown on the etched substrate region is less oriented and experiences strain relief. At the highest temperatures (above 360 K) the entire sample becomes metallic, indicating the quality of the VO_2 film and the robustness of the phase transition even with the etched TiO_2 substrate.

As the dimensions of the pattern are reduced, the effects of the adjacent strain distribution in a specific region of the pattern become increasingly important. This is evident

in the fully bounded unetched substrate regions (UE_b) in Figure 3 (c)-(e) and (h)-(i), where metallic stripes are observed to form at lower temperatures than the isotropic phase change of the etched-substrate patterned region (EP), indicating an intermediate state exists as a result of strain-induced confinement effects. The existence of this intermediate state is most pronounced when the length scales are comparable to the intrinsic limit of the self-organized stripes, in which case the adjacent strain environment influences the phase separation as discussed in the Supplemental Materials. By measuring checkerboard patterns with different lateral sizes and orientations fabricated on the same film, we have reached the following conclusions: regions (UP), (UE), and (UE_b) (as shown in Figure 3) exhibit striped phase coexistence, while region (EP) supports localized nucleation of the metallic state; region (UP) has a higher transition temperature than region (EP) and (UE_b); all regions complete the IMT above 350 K and the signal levels are close to each other at the fully metallic state; and the in-plane orientation of the checkerboard pattern does not play a major role in the mesoscopic phase separation.

The corresponding temperature dependent structural variation across the same checkerboard pattern in Figure 3 (a)-(f) is presented in Figure 4. The x-ray reflectivity data, fit of the component phases, and the peak locations of the component phases as a function of temperature are plotted for region (UP) (Figure 4 (a)-(c)) and region (EP) (Figure 4 (d)-(f)). The x-ray intensity map taken at the VO₂ (022)_M film peak position at 300 K is shown in the inset of Figure 4 (a). Figure 4(a) and (d) show the specular scans measured in the vicinity of the VO₂ (022)_M peak and (220)_R peak as a function of the out-of-plane scattering vector, $Q_z = 4\pi\sin(\theta/2)/\lambda$, where θ is the incident angle and λ is the x-ray wavelength. We find that in regions (UP) and (EP), two sets of monoclinic (022)_M peaks (below ~340 K) and two sets of rutile (220)_R peaks (above ~330K) can be identified. As discussed earlier, at room temperature two monoclinic (022)_M peaks in the x-ray reflectivity, noted as M and M', can be clearly resolved with the fitting. The M peak is close to the bulk value of monoclinic VO₂ (022)_M

peak while the M' peak has a smaller out-of-plane lattice constant. Above ~340 K, two rutile (220)_R peaks R and R' can be identified. The R peak is close to the bulk value while R' has a smaller out-of-plane lattice constant. At 335 K, in the vicinity of phase transition temperature, all four peaks (M, M', R, R') are observed in Figure 4 (b) and 4 (e) as a result of the strain-induced phase separation. Although the absolute intensity of the x-ray reflectivity at region (EP) is much lower compared to that observed at region (UP), the two-peak features in both locations are similar. The vertical lines in Figure 4 (c) and 4 (f) are the calculated Q values - 3.9025 \AA^{-1} and 3.9297 \AA^{-1} - which correspond to the bulk out-of-plane lattice constants 3.1978 \AA (110)_M and 3.2201 \AA (110)_R, respectively [43,44].

The main structural differences between region (UP) and region (EP) are as follows. First, at 335 K, the R phase in region (UP) has an out-of-plane lattice constant slightly larger than the bulk value (Figure 4 (c)). An in-plane lattice constant smaller than the bulk value along the (001)_R axis is expected due to the Poisson effect [45], which explains the occurrence of the metallic stripes in region (UP) below the bulk-T_c (~340 K) [45] as in-plane strain drives the phase separation. In region (EP), the Rutile phase has a slightly smaller lattice constant than the bulk value (Figure 4 (f)) and the occurrence of the metallic nucleation in region (EP) is mostly due to the parts of the VO₂ film with out-of-plane orientations other than (110)_R. The second difference between region (UP) and (EP) is the fraction of the component phases at the same temperature. In region (EP), the R' peak strengthens at a lower temperature than in region (UP), while the R peak strengthens at a higher temperature than in region (UP).

The μ -XRD measurement is consistent with the electronic phase separation and the broad hysteresis of the VO₂ films observed in the near-field images. The alternating relaxed-tensile-relaxed strain environment modulates the VO₂ film crystal structure so that the M, M', R, and R' phases coexist below and above 340 K. This is in agreement with the observation that the metallic and insulating states coexist below and above 340 K in the near-field (imaged as

stripes in the highly oriented region (UP)). The significantly lower XRD intensity and slightly different strain levels in region (EP) compared to region (UP) are in agreement with the expectation that the substrate-etched area has a multi-faceted crystal domain structure, which leads to different metallic domain formation at the mesoscopic scale. This consistency between the near-field and μ -XRD measurements strongly suggests that the modification of the local structural phase coexistence through interface strain nano-engineering can lead to controlled reordering of the phase separation textures in the electronic response.

To explore the feasibility of substrate engineering with even smaller feature sizes, patterns with dimensions less than 5 μm and 1.5 μm have been fabricated (e.g. 1 μm , See Figure S9 [19]). For the $(110)_R$ substrate orientation, we found that the smallest length scale at which one can still reliably distinguish the etched versus unetched region is ~ 250 nm, irrespective of etch depth between 5-110 nm. This can be understood given the fact that the periodicity of the spontaneous strain-induced striped phase separation of a ~ 50 nm thick unpatterned $\text{VO}_2/(110)_R \text{TiO}_2$ film is on the order of 200 nm (see the Supplemental Materials in reference [11]). In other words, the periodicity of the long range ordered, self-organized stripes defines the ultimate ‘resolution’ of the substrate’s impact on the local phase transitions in the films. In $\text{VO}_2/(001)_R \text{TiO}_2$ films, this restriction no longer applies since there is no in-plane anisotropy or conductive stripe state. As a result, the ‘resolution’ of the pattern in $\text{VO}_2/(001)_R \text{TiO}_2$ films is only limited by the resolution of FIB writing, which can be reliably controlled down to 50 nm. We note that patterning a $(001)_R \text{TiO}_2$ substrate leads to the opposite trend in the transition temperature: the VO_2 transition temperature increases in the (EP) region as a result of the out-of-plane c-axis orientation.

In summary, we have demonstrated the feasibility of microscopic substrate engineering in vanadium dioxide thin films. By utilizing pre-patterned substrates to control the local crystal growth and strain environment, we are able to manipulate the composite phases on a

length scale close to the intrinsic self-organized phase separation in thin films without requiring post-fabrication processing. Since the epitaxial strain-induced mesoscopic phase separation phenomenon is rather common in strongly correlated electron materials [14,47–50], this work provides a universal means for controlling the local electronic phase separation, especially in heterostructures systems.

See Supplemental Material at [*URL will be inserted by publisher*] for details on the substrate patterning method, patterned substrate characterization with AFM and Raman, VO₂ film characterization, analysis of the VO₂ surface roughness, full μ -XRD diffraction map and spectra of the 5 μ m x 5 μ m pattern, XRD reciprocal space map of the three sample regions, Raman spectroscopy of the 5 μ m x 5 μ m pattern, XRD analysis of the unpatterned and etched patterned regions, and 2D FFT analysis of the phase separation in the system.

Acknowledgements

The authors gratefully acknowledge the efforts of M. Raschke and his group in developing the SINS instrument at the ALS. I.C. and H. W. acknowledge the support from the U.S Department of Energy, Basic Energy Sciences, Materials Sciences and Engineering Division, under Grant No. DE-SC0012509. The use of APS is supported by the U.S Department of Energy, Office of Science, Office of Basic Energy Sciences under Contract No. DE-AC02-06CH11357. This research used resources of the Advanced Light Source, which is a DOE Office of Science User Facility under contract No. DE-AC02-05CH11231. G. L. Carr acknowledges DOE funding under contract DE-SC0012704 for NSLS-II support at ALS. This work is partially supported by the National Science Foundation under the CMMI Division (Grant No. 1563422, No. 1562915).

Author Contributions

S.N.G.C. and J. J. contributed equally to this work. S.N.G.C., M.K.L., I.C.T, and H. W. wrote the manuscript with all of the authors contributing to editing. S.N.G.C., X.C., and J.Z. performed the near-field measurements. S.N.G.C. and M.K.L. analyzed the near-field data. H.A.B., M.C.M. and G.L.C. provided support and access to the nano-FTIR beamline at ALS. I.C.T, Z.C., Y.Z., and H.W. performed the XRD measurements at APS. I.C.T and H.W. analyzed the XRD data. S.K., J.L., and S.A.W deposited the VO₂ films. S.K. analyzed the Raman data. J.J. and H.T.H. patterned and characterized the TiO₂ substrates. M.K.L, H.T.H., and H.W. designed the experiment.

References

- [1] J. Ge, Z.-L. Liu, C. Liu, C. Gao, D. Qian, Q. Xue, Y. Liu, and J.-F. Jia, *Nat. Mater.* **14**, 285-289 (2014), DOI: 10.1038/NMAT4153.
- [2] M. Li, T. Graf, T. D. Schladt, X. Jiang, and S. S. P. Parkin, *Phys. Rev. Lett.* **109**, 196803 (2012), DOI: 10.1103/PhysRevLett.109.196803.
- [3] A. D. Caviglia, S. Gariglio, N. Reyren, D. Jaccard, T. Schneider, M. Gabay, S. Thiel, G. Hammerl, J. Mannhart, and J.-M. Triscone, *Nature* **456**, 624-627 (2008), DOI: 10.1038/nature07576..
- [4] M. D. Goldflam, T. Driscoll, D. Barnas, O. Khatib, M. Royal, N. M. Jokerst, D. R. Smith, B. Kim, G. Seo, H.-T. Kim, and D. N. Basov, *Appl. Phys. Lett.* **102**, 224103 (2013), DOI: 10.1063/1.4809534.
- [5] M. D. Goldflam, M. K. Liu, B. C. Chapler, H. T. Stinson, A. J. Sternbach, A. S. McLeod, J. D. Zhang, K. Geng, M. Royal, B. J. Kim, R. D. Averitt, N. M. Jokerst, D. R. Smith, H. T. Kim, and D. N. Basov, *Appl. Phys. Lett.* **105**, 041117 (2014), DOI 10.1063/1.4891765.

- [6] J. Rensberg, S. Zhang, Y. Zhou, A. S. McLeod, C. Schwarz, M. Goldflam, M. Liu, J. Kerbusch, R. Nawrodt, S. Ramanathan, D. N. Basov, F. Capasso, C. Ronning, and M. A. Kats, *Nano Lett.* **16**, 1050-1055 (2016), DOI: 10.1021/acs.nanolett.5b04122.
- [7] M. K. Liu, B. Pardo, J. Zhang, M. M. Qazilbash, S. J. Yun, Z. Fei, J. H. Shin, H. T. Kim, D. N. Basov, and R. D. Averitt, *Phys. Rev. Lett.* **107**, 066403 (2011), DOI: 10.1103/PhysRevLett.107.066403.
- [8] M. Liu, H. Y. Hwang, H. Tao, A. C. Strikwerda, K. Fan, G. R. Keiser, A. J. Sternbach, K. G. West, S. Kittiwatanakul, J. Lu, S. A. Wolf, F. G. Omenetto, X. Zhang, K. A. Nelson, and R. D. Averitt, *Nature* **487**, 345-348 (2012), DOI: 10.1038/nature11231.
- [9] J. Zhang, X. Tan, M. Liu, S. W. Teitelbaum, K. W. Post, F. Jin, K. A. Nelson, D. N. Basov, W. Wu, and R. D. Averitt, *Nat. Mater.* **15**, 956 (2015), DOI: 10.1038/NMAT4695.
- [10] M. Liu, A. J. Sternbach, M. Wagner, T. V. Slusar, T. Kong, S. L. Bud, S. Kittiwatanakul, M. M. Qazilbash, A. McLeod, Z. Fei, E. Abreu, J. Zhang, M. Goldflam, S. Dai, G. Ni, J. Lu, H. A. Bechtel, M. C. Martin, M. B. Raschke, R. D. Averitt, S. A. Wolf, H. Kim, P. C. Canfield, and D. N. Basov, *Phys. Rev. B* **91**, 245155 (2015), DOI: 10.1103/PhysRevB.91.245155.
- [11] M. K. Liu, M. Wagner, E. Abreu, S. Kittiwatanakul, A. S. McLeod, Z. Fei, M. D. Goldflam, S. Dai, M. M. Fogler, J. Lu, S. A. Wolf, R. D. Averitt, D. N. Basov, *Phys. Rev. Lett.* **111**, 96602 (2013), DOI: 10.1103/PhysRevLett.111.096602.
- [12] J. Laverock, S. Kittiwatanakul, A. A. Zakharov, Y. R. Niu, B. Chen, S. A. Wolf, J. W. Lu, and K. E. Smith, *Phys. Rev. Lett.* **113**, 216402 (2014), DOI: 10.1103/PhysRevLett.113.216402.
- [13] M. Liu, A. J. Sternbach, and D. N. Basov, *Reports Prog. Phys.* **80**, 14501 (2017), DOI: 10.1088/0034-4885/80/1/014501.
- [14] K. Lai, M. Nakamura, W. Kundhikanjana, M. Kawasaki, Y. Tokura, M. A. Kelly, and

- Z.-X. Shen, *Science* **329**, 190-193 (2010) , DOI: 10.1126/science.1189925.
- [15] M. Liu, M. Wagner, J. Zhang, A. McLeod, S. Kittiwatanakul, Z. Fei, E. Abreu, M. Goldflam, A. J. Sternbach, S. Dai, K. G. West, J. Lu, S. A. Wolf, R. D. Averitt, and D. N. Basov, *Appl. Phys. Lett.* **104**, 121905 (2014), DOI: 10.1063/1.4869558.
- [16] T. Yajima, Y. Ninomiya, T. Nishimura, and A. Toriumi, *Phys. Rev. B* **91**, 205102 (2015), DOI: 10.1103/PhysRevB.91.205102.
- [17] M. M. Qazilbash, M. Brehm, B.-G. Chae, P.-C. Ho, G. O. Andreev, B.-J. Kim, S. J. Yun, A. V. Balatsky, M. B. Maple, F. Keilmann, H.-T. Kim, and D. N. Basov, *Science* **318**, 1750-1753 (2007), DOI: 10.1126/science.1150124.
- [18] M. M. Qazilbash, M. Brehm, G. O. Andreev, A. Frenzel, P. C. Ho, B.-G. Chae, B.-J. Kim, S. J. Yun, H.-T. Kim, A. V Balatsky, O. G. Shpyrko, M. B. Maple, F. Keilmann, and D. N. Basov, *Phys. Rev. B* **79**, 75107 (2009), DOI: 10.1103/PhysRevB.79.075107.
- [19] See Supplemental Material at [URL will be inserted by publisher] for details on the substrate patterning method, patterned substrate characterization with AFM and Raman, VO₂ film characterization, analysis of the VO₂ surface roughness, full μ -XRD diffraction map and spectra of the 5 μ m x 5 μ m pattern, XRD reciprocal space map of the three sample regions, Raman spectroscopy of the 5 μ m x 5 μ m pattern, XRD analysis of the unpatterned and etched patterned regions, and 2D FFT analysis of the phase separation in the system.
- [20] Y. Greenzweig, Y. Drezner, S. Tan, R. H. Livengood, and A. Raveh, *Microelectron. Eng.* **155**, 19-24 (2016), DOI: 10.1016/j.mee.2016.01.016.
- [21] F. Hofmann, E. Tarleton, R. J. Harder, N. W. Phillips, P.-W. Ma, J. N. Clark. I. K. Robinson, B. Abbey, W. Liu, C. E. Beck, *Sci. Rep.* **7**, 45993 (2017), DOI: 10.1038/srep45993.
- [22] S. Kittiwatanakul, J. Laverock, D. Newby Jr, K. E. Smith, S. A. Wolf, and J. Lu, J.

- Appl. Phys. **114**, 53703 (2013) , DOI: 10.1063/1.4817174.
- [23] K. G. West, J. Lu, J. Yu, D. Kirkwood, W. Chen, Y. Pei, J. Claassen, and S. A. Wolf, J. Vac. Sci. Technol. A Vacuum, Surfaces, Film. **26**, 133 (2008), DOI: 10.1116/1.2819268.
 - [24] D. Bonnell, D. Basov, M. Bode, U. Diebold, S. Kalinin, V. Madhavan, L. Novotny, M. Salmeron, U. Schwarz, and P. Weiss, Rev. Mod. Phys. **84**, 1343-1381 (2012), DOI: 10.1103/RevModPhys.84.1343.
 - [25] J. M. Atkin, S. Berweger, A. C. Jones, and M. B. Raschke, Adv. Phys. **61**, 745-842 (2012), DOI: 10.1080/00018732.2012.737982.
 - [26] D. A. Powell, M. Lapine, M. V. Gorkunov, I. V. Shadrivov, and Y. S. Kivshar, Phys. Rev. B **82**, 155128 (2010), DOI: 10.1103/PhysRevB.82.155128.
 - [27] B. Knoll, and F. Keilmann , Nature **399**, 134-137 (1999), DOI: 10.1038/20154.
 - [28] F. Keilmann, A. J. Huber, and R. Hillenbrand, J. Infrared, Millimeter, Terahertz Waves **30**, 1255 (2009), DOI 10.1007/s10762-009-9525-3.
 - [29] S. Amarie, T. Ganz, and F. Keilmann, Opt. Express **17**, 21794-21801 (2009), DOI: 10.1364/OE.17.021794.
 - [30] R. M. Bakker, V. P. Drachev, H. K. Yuan, and V. M. Shalaev, Phys. B Condens. Matter **394**, 137-140 (2007), DOI: 10.1016/j.physb.2006.12.045.
 - [31] A. J. Huber, F. Keilmann, J. Wittborn, J. Aizpurua, and R. Hillenbrand, Nano Lett. **8**, 3766-3770 (2008), DOI: 10.1021/nl802086x.
 - [32] H. A. Bechtel, E. A. Muller, R. L. Olmon, M. C. Martin, and M. B. Raschke, Proc. Natl. Acad. Sci. U. S. A. **111**, 7191 (2014), DOI: 10.1073/pnas.14005021.
 - [33] J. Pendry, Opt. Photonics News **15**, 33 (2004), DOI: 10.1364/OPN.15.9.000032.
 - [34] M. Schnell, A. García-Etxarri, A. J. Huber, K. Crozier, J. Aizpurua, and R. Hillenbrand, Nat. Photonics **3**, 287 (2009), DOI:10.1038/nphoton.2009.46.
 - [35] M. Schnell, A. Garcia-Etxarri, J. Alkorta, J. Aizpurua, and R. Hillenbrand, Nano Lett.

- 10**, 3524 (2010), DOI: 10.1021/nl101693a.
- [36] N. Kumar, A. C. Strikwerda, K. Fan, X. Zhang, R. D. Averitt, P. C. M. Planken, and A. J. L. Adam, Opt. Express **20**, 11277 (2012), DOI:10.1364/OE.20.011277.
 - [37] Y. Zhu, Z. Cai, P. Chen, Q. Zhang, M. J. Highland, I. W. Jung, D. A. Walko, E. M. Dufresne, J. Jeong, M. G. Samant, S. S. P. Parkin, J. W. Freeland, P. G. Evans, and H. Wen, Sci. Rep. **6**, 21999 (2016), DOI: 10.1038/srep21999.
 - [38] T. J. Huffman, P. Xu, M. M. Qazilbash, E. J. Walter, H. Krakauer, J. Wei, D. H. Cobden, H. A. Bechtel, M. C. Martin, G. L. Carr, and D. N. Basov, Phys. Rev. B **87**, 115121 (2013), DOI: 10.1103/PhysRevB.87.115121.
 - [39] P. Colomban, A. Slodczyk, Opt. Mater. **31**, 1759-1763 (2009).
 - [40] K. Shirai, Y. Moriguchi, M. Ichimura, A. Usami, M. Saji, Jpn. J. Appl. Phys. **35**, L1483 (1996).
 - [41] C. Marini, E. Arcangeletti, D. Di Castro, L. Baldassare, A. Perucci, S. Lupi, L. Malavasi, L. Boeri, E. Pomjakushina, K. Conder, P. Postorino, Phys. Rev. B **77**, 235111, (2008).
 - [42] S. Kittiwatanakul, S. A. Wolf, J. Lu, Appl. Phys. Lett. **105**, 073112, (2014).
 - [43] Y. Muraoka and Z. Hiroi, Appl. Phys. Lett. **80**, 583 (2002), DOI: 10.1063/1.1446215.
 - [44] G. Andersson, Acta Chem. Scand. **8**, 1599 (1954), DOI: 10.3891/acta.chem.scand.08-1599.
 - [45] J. Pelleg, *Mechanical Properties of Materials. Springer Series Solid Mechanics and Its Applications* (2013).
 - [46] B. Lazarovits, K. Kim, K. Haule, and G. Kotliar, Phys. Rev. B **81**, 115117 (2010), DOI: 10.1103/PhysRevB.81.115117.
 - [47] A. S. McLeod, E. van Heumen, J. G. Ramirez, S. Wang, T. Saerbeck, S. Guenon, M. Goldflam, L. Anderegg, P. Kelly, A. Mueller, M. K. Liu, I. K. Schuller, and D. N. Basov, Nat. Phys. **13**, 80-86 (2017), DOI: 10.1038/nphys3882.

- [48] E. Dagotto, T. Hotta, and A. Moreo, Phys. Rep. **344**, 1 (2001), DOI: 10.1016/S0370-1573(00)00121-6.
- [49] N. D. Mathur and P. B. Littlewood, Phys. Today **56**, 25 (2003), DOI: 10.1063/1.1554133.
- [50] E. Dagotto, Science **309**, 257 (2005), DOI: 10.1126/science.1107559.

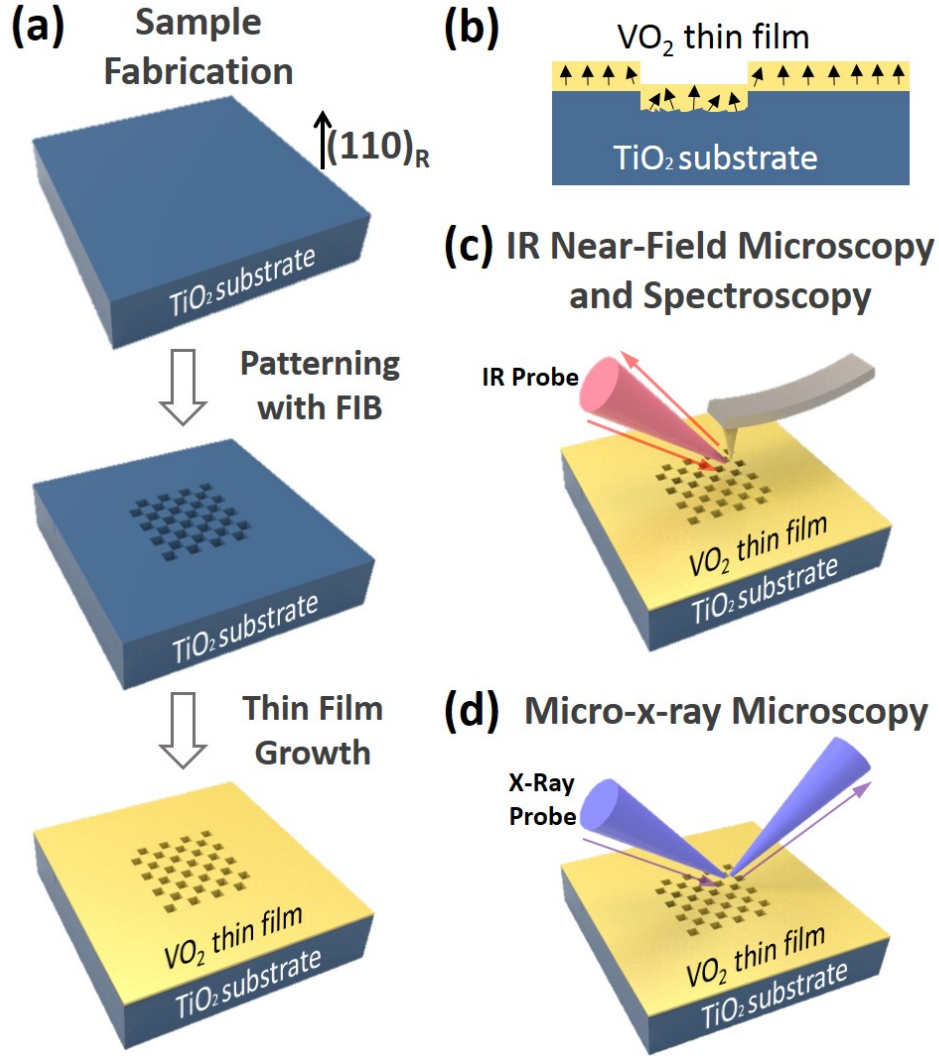


Fig 1. (Color online) Experimental Design. (a) The samples are fabricated by patterning TiO₂ (110)_R substrates with a focused ion beam to produce a checkerboard pattern. After patterning, a VO₂ thin film (~71 nm) is grown over the substrate. The strain relief caused by the patterning of the substrate locally disrupts the VO₂ overgrowth, producing microscopic regions of different crystallinity. (b) Schematic cross section of the VO₂/TiO₂ interface showing the effects of etching and structural modification. The growth on the patterned regions produces a less coherent VO₂ film as different TiO₂ crystal facets are exposed by etching. (c) The local electronic phase transitions of the patterned samples are investigated with imaging and broadband spectroscopic s-SNOM with ~10 nm resolution. (d) The local crystallinity and structural phase transition of the VO₂ film are explored with micro-XRD with ~1 μ m resolution.

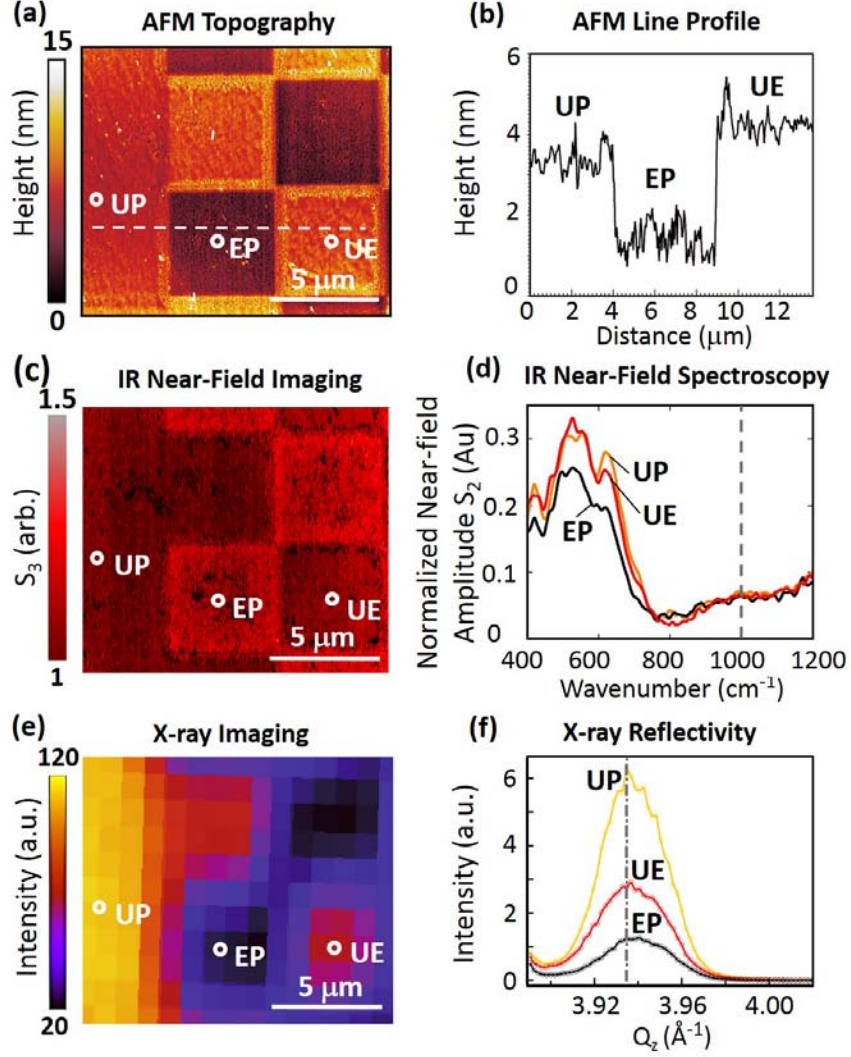


Fig 2. (Color online) Near-field nano-spectroscopy and micro-x-ray diffraction at room temperature. (a) AFM topography at the edge of a checkerboard pattern with $5\ \mu\text{m} \times 5\ \mu\text{m}$ boxes. Three distinct locations on the pattern are identified: (UP) unpatterned region, (UE) unetched-substrate patterned region, and (EP) etched-substrate patterned region. (b) Topography profile along the white dashed line in a). (c) Room temperature near-field image collected at $\sim 10\ \mu\text{m}$ showing the IR response of the same pattern as in a). (d) Broadband near-field spectra (referenced to gold) collected at each of the regions identified in (a) and (c), showing a shift in the phonon amplitude within the patterned region (curve EP). The unpatterned regions (as indicated by curve UP and UE) show nearly identical responses. The vertical dashed line indicates the $10\ \mu\text{m}$ wavelength where the near-field image (c) was collected. (e) Room temperature μ -XRD intensity map where the diffraction intensity at the monoclinic (022)_M Bragg peak position has been used to generate the contrast. (f) Specular scans measured at various locations as labeled in (e).

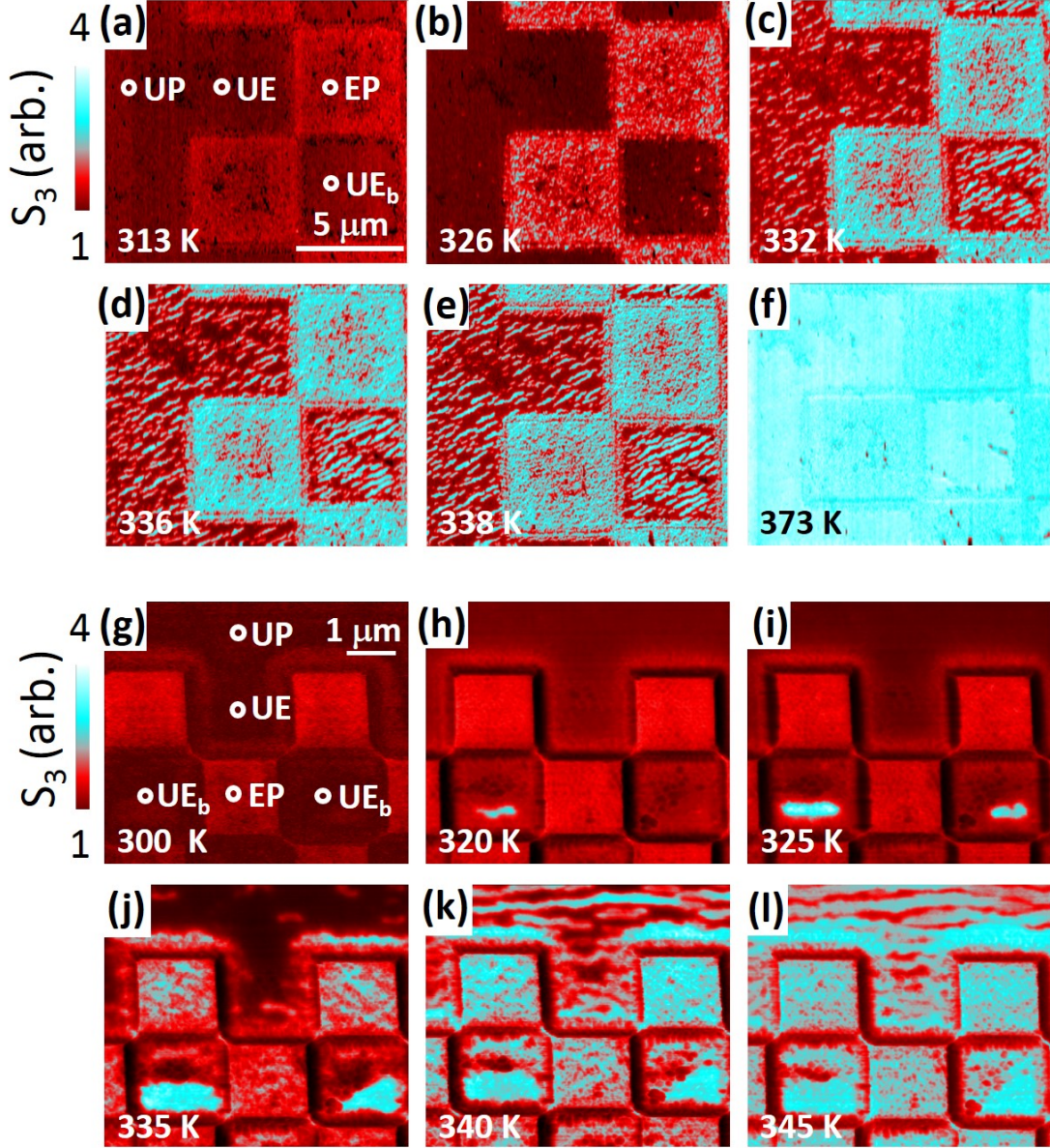


Fig 3. (Color online) Temperature-dependent infrared near-field images of patterned VO_2/TiO_2 at $11\ \mu\text{m}$, revealing area-dependent insulator to metal phase transitions. The metallic phase is shown in cyan and the insulating phase is in red. (a)-(f), $5\ \mu\text{m} \times 5\ \mu\text{m}$ checkerboard patterns at (a) 313 K, (b) 326 K, (c) 332 K, (d) 336 K, (e) 338 K, (f) 373 K. (g)-(l), $1.5\ \mu\text{m} \times 1.5\ \mu\text{m}$ checkerboard patterns on the same sample, at (g) 300 K, (h) 320 K, (i) 325 K, (j) 335 K, (k) 340 K, (l) 345 K. The smaller scale of the pattern shown in (g)-(l) exhibits strain-induced confinement effects, especially in the fully bounded UE regions (UE_b).

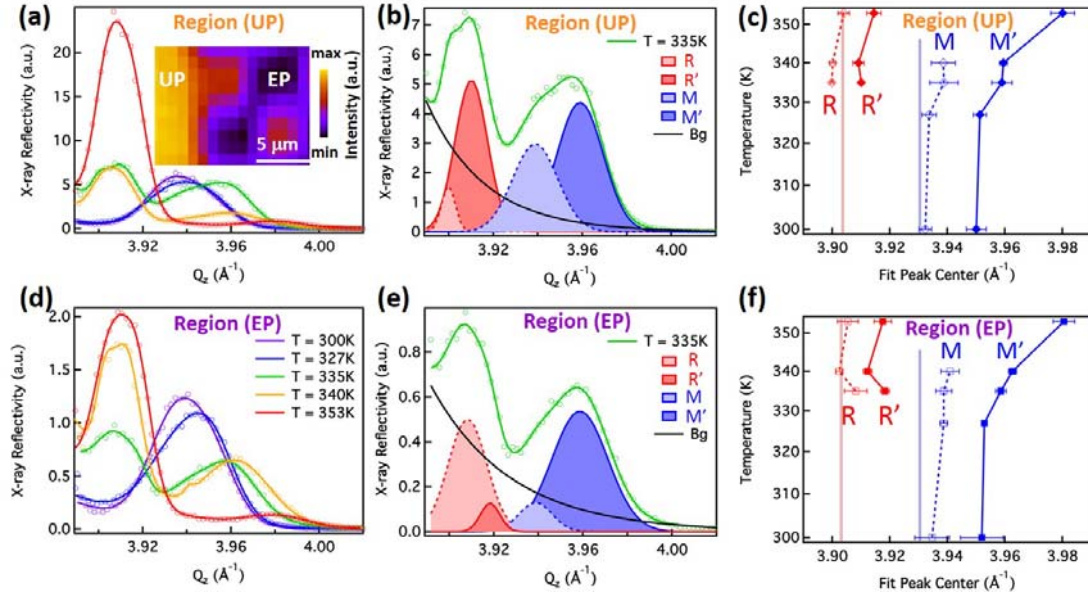


Fig 4. (Color online) μ -XRD analysis of the VO_2/TiO_2 patterned area. Micro-XRD intensity map taken at the film peak position at 300 K is shown in the inset of (a). The measurements in region (UP) are summarized in (a) the specular x-ray diffraction scans at various temperatures corresponding to the legend in (d), (b) the representative fitting of diffraction peaks at $T=335\text{ K}$, and (c) the extracted temperature-dependent Bragg peak positions. (d)-(f) Show the corresponding plots for region (EP).